34th Annual International Conference of the IEEE EMBS
San Diego, California USA, 28 August - 1 September, 2012

Tracking and Position Control of an MRI-Powered Needle-Insertion Robot

Christos Bergeles, *Member, IEEE*, Lei Qin, Panagiotis Vartholomeos, *Member, IEEE*, and Pierre E. Dupont, *Fellow, IEEE*

***Abstract*— The excellent imaging capabilities of MRI technology are standardizing this modality for a variety of interventional procedures. To assist radiologists, MRI compatible robots relying on traditional actuation technologies are being developed. Recently, a robot that is not only MRI compatible but also MRI powered was introduced. This surgical robot is imaged and actuated through interleaved MRI pulses, and can be controlled to perform automated needle insertion. Using the electromagnetic field generated by the MRI scanner, the robot can exercise adequate forces to puncture tissue. Towards the goal of automation, this paper reports results on tracking and control of an MRI-powered robot tagged with a fiducial marker. Tracking is achieved using non-selective RF pulses and balanced gradient readouts. To suppress the signal received from the tissue, spoiler gradients and background suppression are introduced. Their effects on tracking are quantified and are used to optimize the algorithm. Subsequently, a Kalman filter is employed for robustness. The developed algorithm is used to demonstrate position controlled needle insertion *ex vivo*.**

I. Introduction

Computed tomography (CT), X-ray fluoroscopy and ultrasound are the most commonly used intraoperative imaging modalities. CT and X-ray fluoroscopy offer high quality images, but their ionizing radiation can be harmful to the patient. On the other hand, ultrasound is safe but cannot provide high resolution images. None of these issues are present in MR imaging, which provides high-quality images using non-ionizing radiation. The use of a surgical robot inside an MRI scanner poses unique challenges, however, because standard robot components can produce dangerous forces and torques and degrade image quality.

A variety of promising surgical robots incorporating these constraints have been developed [1]. Robots for assistance in prostate brachytherapy were reported in [2], [3], while [4] presented a meso-scale robot for neurosurgical interventions. These robots rely on MRI-compatible components and common actuation techniques [5]. Alternatively, a recent trend is the exploration of wirelessly generated forces to either augment or replace mechanically transmitted forces. For example, electromagnetic systems have been used to wirelessly power intraocular microrobots [6], and MRI systems have been used for the propulsion of flagellated endoscopes [7] and endovascular drug-carriers [8].

This work was supported by the Wyss Institute for Biologically Inspired Engineering and by the National Institutes of Health under grant R01HL073647.

C. Bergeles, P. Vartholomeos, and P. E. Dupont are with Cardiovascular Surgery, Children's Hospital Boston, Harvard Medical School, Boston MA, 02115, USA {firstname.lastname}@childrens.harvard.edu. Lei Qin is with Dana Farber Cancer Research, Boston MA, 02115, USA {lqin2@partners.org}.

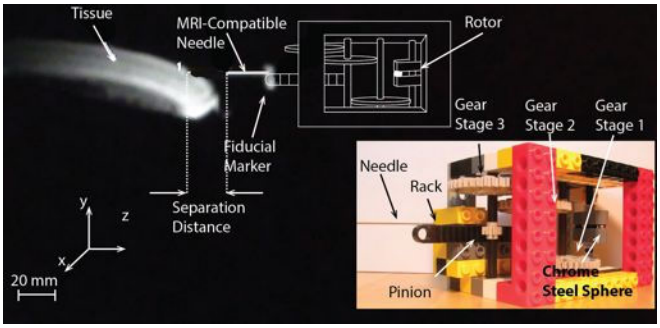

Fig. 1. Illustration of the MRI-actuated robot. The image indicates the gear system, the rack and the needle. The fiducial marker that is used for tracking is attached on the rack. Through the rotation of the magnetic field gradients of the MRI, motion is induced to the chrome-steel bead, and this motion is transferred through a series of gears to the needle. The robot is MRI-compatible, and thus invisible in the image. The illustration is composed of a schematic of the device overlaid on its MRI scan.

By combining wireless force generation and MRI compatibility, we introduced the concept of MRI-powered robotic actuators and reported our first results on an MRI-powered robot in [9]. The current paper reports progress on device tracking and control, together with an automated needle insertion experiment in *ex vivo* tissue. Section II provides brief details on the actuation methodology, and Sec. III introduces the tracking algorithm and the effects of using spoiler gradients and background suppression. Section IV discusses the implementation of a Kalman filter and showcases its benefits, and Sec. V demonstrates a needle-driving procedure with MRI-tracking and powering. The paper concludes with a discussion in Sec. VI.

II. MRI-Actuated Needle-Insertion Robot

The actuator is comparable to an electric motor. It consists of the stator, which comprises the MRI scanner and the stationary components of the actuator, and a rotor, which is the rotating portion of the actuator (see Fig. 1). The rotor contains a ferrous sphere enclosed in a cavity which is located at the maximum possible moment arm to provide maximum torque. Rotation of the rotor is generated by applying magnetic gradients to generate a force $\vec{F}$ on the ferromagnetic sphere. The actuator is placed near the isocenter of the scanner so that the rotor's plane of rotation coincides with the X-Z plane of the scanner reference frame. The maximum gradient of a clinical MRI is $40\,\mathrm{mT/m}$, which leads to small actuation forces (on the order of $10\,\mathrm{mN}$ for

magnetic volumes of few mm^3). This limitation is addressed using a gear-train ($125:1$), together with a rack and pinion, to provide linear motion and interventional-level forces [9]. An MRI-compatible biopsy needle is attached on the rack.

The actuator prototype has been constructed using LEGO components [see Fig. 1(inlet)] because they offer a fast, easy, and reliable way to build MRI-compatible mechanisms. All components are plastic except for the biopsy needle, which is made of (non-ferromagnetic) titanium (Chiba MReye, Cook Medical), and the (ferromagnetic) chrome steel sphere. The dimensions of this prototype are $10 \times 6 \times 6$ cm. The force capabilities of the prototypical device have been tested in a clinical 1.5 T GE scanner, where it was shown that the rack can apply forces up to 1 N, which allowed open-loop puncture of a porcine heart [9].

III. Fiducial Marker Tracking

For decreased complexity and to allow for a wireless and untethered robotic mechanism, passive marker tracking is considered. Typically, in passive tracking, paramagnetic particles used as fiducial markers are detected in reconstructed MRI images [10], [11]. Tracking using the reconstructed images does not allow a high throughput. For example, as reported in [12], one of the fastest imaging sequences, TrueFISP, can create an image not faster than every 0.4 s.

High throughput is crucial when the generation of quick actuation pulses is required. In research that utilizes the MRI scanner for wireless actuation, tracking using single-dimensional projections is considered and particles are localized using projections acquired in 3 axes. For example, [8] uses magnetic-signature-selective RF pulses and gradient-echo pulses to localize an untethered ferromagnetic particle.

When magnetic particles are involved, either as the robots themselves or as part of a mechanism, gradient-echo pulses are preferable since they do not contribute net motion. In our tracking algorithm, the localization pulse sequence consists of a non-selective radio-frequency (RF) pulse followed by a balanced gradient-echo along each axis. The localization sequence is interleaved with the sinusoidal-gradient pulse sequence that powers the robot (see Fig. 2). The localization pulse may follow one or more actuation pulses. The tracked fiducial is an 8 mm-wide MR-SPOTS marker (Beekley Medical, CT) that is attached to the rack of the robot.

In the absence of tissue, the marker creates a strong signal in the single-dimensional spatially encoded projection, and the peak of the signal is selected as its location [see Fig. 3(a)]. The peak can be detected using peak-finding, preferred here, or correlation methods [8], [13]. The estimated position may be affected by spatial quantization and noise.

In the presence of tissue, the marker's relative signal intensity is considerably less [see Fig. 3(b)]. It can only be detected along the axis of motion of the needle, which is the direction of interest. In the remaining directions, the tissue and marker cannot be differentiated using single-dimensional spatial encoding. In order to suppress the intensity of the signal emanating from the tissue, we introduce spoiler and rewinder gradients in the imaging pulse sequence (see Fig. 2). Spoilers dephase the magnetization, and the tissue, being larger than the marker, gets its signal suppressed. Rewinders act after the signal readout to rephase the spins that are dephased by the spoiler. To estimate their effect of spoilers on localization, a series experiments were performed.

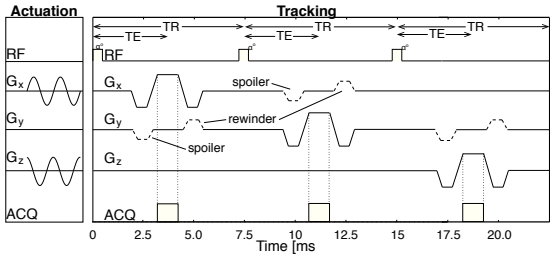

Fig. 2. The tracking pulse sequence: the dashed-line indicates the spoiler gradient that is used for suppressing the signal emitted from the tissue. The localization gradient is repeated on each axis. Parameters: TE = 3 ms, TR = 7.5 ms, $\alpha = 5°$, field-of-view = 300 mm, bandwidth = ± 64 KHz, matrix = 512 voxels, amplitude = 40 mT/m.

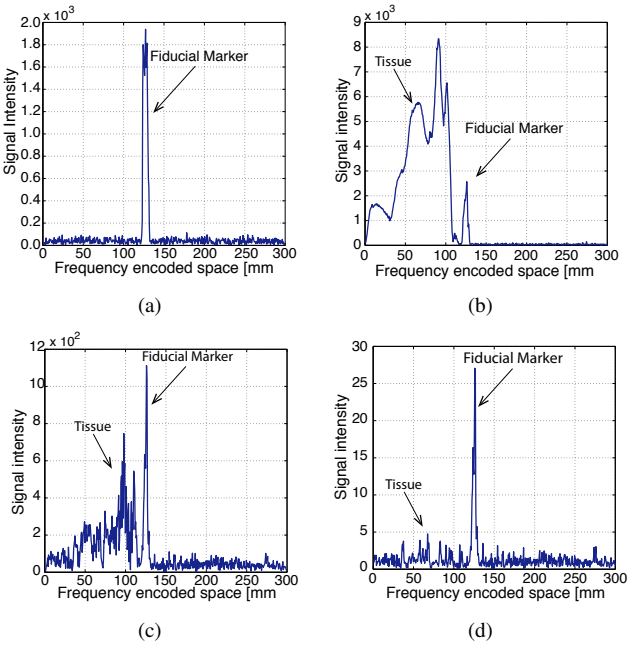

Fig. 3. Different cases of signal detection: (a) In the absence of tissue, the MR-SPOTS marker gives a high signal whose peak indicates its location. (b) In the presence of tissue, the signal of the marker is shadowed by the signal of the tissue. (c) Spoiler gradients suppress the tissue signal, but induce noise in the overall signal as well. (d) Background suppression leads to excellent marker signal intensity with a gaussian profile.

In a 1.5 T GE scanner, spoiler gradient amplitudes ranging from 0% to 100% of the maximum gradient amplitude (40 mT/m) were examined. A marker was placed in 5 known positions separated by 20 mm, and its location was estimated 10 times. The emitted signal was transferred in real-time to our image-processing and control workstation using RTHawk [14]. The spatial signal resolution was calculated at $585\,\mu$m.

As Fig. 3(c) shows, the spoiler gradients indeed suppress the tissue's signal, but noisy peaks are introduced. Thus, it is not possible to robustly localize the marker solely through the use of spoilers.

To tackle this problem, we introduce background suppression. The single-dimensional tissue signal response can be captured in the absence of the marker, in a procedure preceding the introduction of the MRI-powered robot in the scanner bore. Then, during the intervention, the tissue profile is used in a background suppression algorithm to amplify the signal received from the marker:

$$S' = \frac{S}{B + \epsilon} \tag{1}$$

where S' is the amplified signal, B is the calculated background, and $\epsilon = 0.1$ is a constant to avoid division by zero. Figure 3(d) shows that this background suppression method can result in low-noise gaussian looking profiles for the marker. Standard background subtraction (i.e., $S' = |S - B|$) is inapplicable because the background varies during the tracking cycle and S' demonstrates false peaks.

The localization experiment reported previously was repeated to quantify the effect of background suppression and spoilers in localization. A series of 10 tissue profiles were used to extract a mean background signal at each spoiler amplitude, and, in the tracking phase, the amplified signal was used. Motivated by the gaussian profile of the new marker signal, three peak detection algorithms were examined: (a) simple peak detection using the maximum signal value, (b) peak detection using the average value in a window covering the 45% highest marker signal, and (c) the mean value of a gaussian function fitted to the 45% highest signal values. Methods (a), (b) showed very similar results, and, so, only method (a) is reported (see Table I).

The experiments show that spoiler gradients are beneficial for localization only at low amplitudes. For high amplitudes (e.g., 20% in our experiments), they introduce noise to the signal, and lead to the suppression of the marker signature until it is no longer visible. Additionally, Table I shows that even though simple peak detection using the maximal signal values has high precision, its accuracy is limited and leads to high mean localization errors. On the other hand, gaussian fitting leads to accurate and precise estimates when no spoilers are used, but should be avoided in the presence of spoiler gradients. This surprising result can be explained by considering that the noise introduced by spoiler gradients makes the gaussian-fitting process numerically unstable.

Based on Table I, we decided to incorporate gaussian fits in the tracking framework in order to achieve higher accuracy without the need of calibration. Thus, we opted for localization with background suppression, no spoiler gradients, and gaussian fitting on the signal profile.

IV. Kalman Filtering

A Kalman filter is introduced to overcome the limitations introduced by spatial signal resolution and tracking imprecision and to create a more robust localization algorithm that can be used for control. According to Sec. II, the velocity of the rack is linearly dependent on the rotational frequency of the gradient magnetic fields. This leads to a simple equation

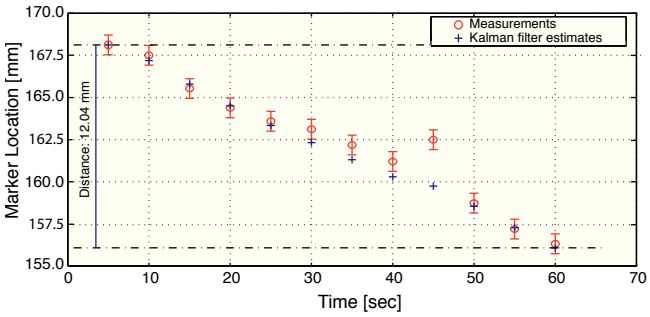

Fig. 4. Localization of the marker using Kalman filtering. The blue crossed represent the outputs of the kalman filter, the red circles the marker positions as estimated by the tracker, and the error bars the resolution of the system.

for the Kalman filter:

$$x_{k+1} = x_k + (\mathrm{u} \times \delta t) \times f \tag{2}$$

$$y_{k+1} = x_{k+1} \tag{3}$$

where k is the sample index, x [m] is the state variable corresponding to the position, $\mathrm{u} = 250\,\mu$m/(sHz) is the velocity of the rack at 1 Hz, f [Hz] is the rotational frequency of the gradients, δt [s] is the tracking interval, and y [m] is the measured position. More information on the kinematics of the robot and their validation are found in [9].

The Kalman filter requires an estimate of the measurement noise and an estimate of the noise in the input variable f. We can consider the spatial resolution ($585\,\mu$m) as measurement noise. The input noise is dependent on the lag that the rotor exhibits with respect to the angle of the electromagnetic field gradients at the time of tracking. This lag is a function of the load and friction, and it could vary between $15° - 90°$, when instability occurs [9]. To account for this lag, we assume an input error of 10% at each tracking cycle.

The performance of the final algorithm is evaluated using the mechanism of Fig. 1 and an actuation frequency of 1 Hz. Localization is performed every 5 actuation cycles. The results are shown in Fig. 4, where it can be seen that the introduction of the Kalman filter leads to better estimates of the marker's location.

V. Experimental Biopsy Procedure

To showcase a practical closed-loop example, we performed a final experiment involving the insertion of an MRI-compatible needle in chicken breast tissue using the MRI-powered actuator. Figure 5(a) shows an MR image acquired using gradient-echo imaging, wherein a 10 mm to-be-traveled-distance is selected. The traversal of the distance is monitored by the localization algorithm, which stops the motion when the location is reached (see Fig. 5(b)).

VI. Conclusions and Future Work

MRI enables wireless power transfer and control while providing high resolution imaging. Tracking in high bandwidths, however, is challenging. We achieved this by using passive markers to track the linear motion of a needle mounted on an MRI-powered robot. We reported how gaussian fitting, spoiler gradients, and background suppression

TABLE I

LOCALIZATION WITH BACKGROUND SUPPRESSION (VALUES IN [MM]).

Location	Spoiler and Rewinder Amplitude 0.00	0.20	0.40	0.60	0.80	1.00	Ground Truth
	Method (a): Peak Detection Using the Maximum Signal Value						
#1	207.42 ± 0.00	207.42 ± 0.00	196.48 ± 35.86	206.74 ± 1.14	110.99 ± 38.86	101.12 ± 38.88	207.0
#2	185.74 ± 0.00	183.64 ± 0.85	186.33 ± 1.06	92.26 ± 48.32	112.94 ± 46.25	96.97 ± 34.43	187.0
#3	161.72 ± 0.00	162.80 ± 2.51	163.09 ± 0.58	156.93 ± 28.02	97.11 ± 22.72	111.33 ± 37.60	167.0
#4	143.55 ± 0.00	143.55 ± 0.00	140.62 ± 0.00	130.86 ± 18.86	132.47 ± 20.12	128.61 ± 22.42	147.0
#5	124.80 ± 0.00	126.22 ± 1.18	125.98 ± 0.00	125.54 ± 1.09	125.24 ± 1.90	111.62 ± 18.42	127.0
Overall	$\underline{2.42 \pm 0.00}$	$\underline{2.44 \pm 0.91}$	4.50 ± 7.50	24.53 ± 19.49	51.25 ± 25.97	57.07 ± 30.35	
	Method (c): Peak Detection Using Gaussian Profile						
# 1	207.76 ± 1.04	198.73 ± 29.02	127.98 ± 42.55	127.15 ± 88.96	152.98 ± 71.79	123.47 ± 61.04	207.0
# 2	185.30 ± 0.36	127.64 ± 43.16	122.46 ± 49.65	108.08 ± 84.69	142.29 ± 76.08	92.87 ± 85.99	187.0
# 3	165.82 ± 0.94	143.60 ± 15.96	137.70 ± 28.49	152.64 ± 55.27	91.62 ± 55.97	122.46 ± 79.50	167.0
# 4	145.85 ± 3.51	141.89 ± 1.35	143.98 ± 5.89	152.25 ± 44.15	141.50 ± 33.47	118.41 ± 46.60	147.0
# 5	125.20 ± 0.29	125.78 ± 3.13	125.59 ± 2.39	124.51 ± 10.47	117.62 ± 44.59	132.47 ± 22.34	127.0
Overall	$\underline{1.32 \pm 1.22}$	19.47 ± 18.52	35.46 ± 25.79	36.17 ± 56.71	37.80 ± 56.38	51.25 ± 59.01	

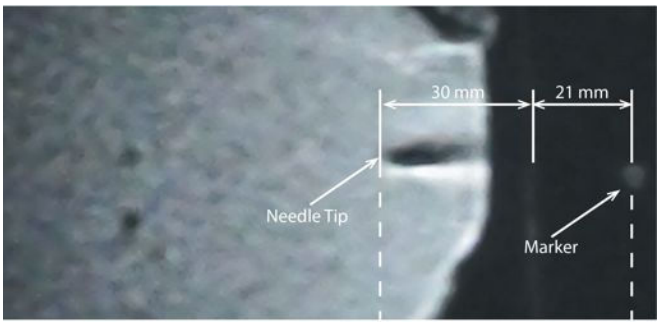

(a)

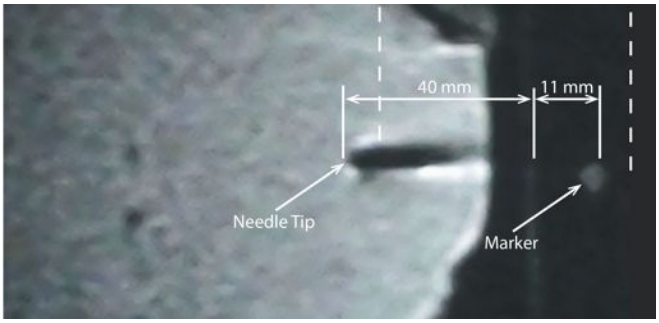

(b)

Fig. 5. An automated needle-insertion scenario using the MRI-powered actuator equipped with an MRI-compatible biopsy needle. Needle was commanded to move for 10 mm, and the tracker halted its motion when it detected a translation of 9.95 mm. Images were taken using a gradient-echo sequence (TE = 2.4 ms, TR = 6.7 ms, bandwidth = ± 31.3 KHz, $\alpha = 30^\circ$). Localization was performed every 5 actuation cycles, leading to 1.25 mm expected steps. (a) Before needle insertion (needle is lying above the tissue), and (b) after needle insertion.

affect the detection of a fiducial marker, and demonstrated the benefits of introducing a Kalman filter in the process. The precision of the localization algorithm allowed performance of a simple needle insertion, which was showcased using an MRI-compatible needle and phantom tissue.

Our future work will be directed towards tracking the rotor motion as well, in order to implement closed-loop commutation control.

REFERENCES

[1] N. V. Tsekos, A. Khanicheh, E. Christoforou, and C. Mavroidis, "Magnetic resonance compatible robotic and mechatronic systems for image-guided interventions and rehabilitation: a review study," *Annual Review of Biomedical Engineering*, vol. 9, pp. 351–387, 2007.

[2] D. Y. Song, E. C. Burdette, J. Fienne, E. Armour, G. Kronreif, A. Deguet, Z. Zhang, I. Iordachita, G. Ficthinger, and P. Kazanzides, "Robotic needle guide for prostate brachytherapy: clinical testing of feasibility and performance," *Brachytherapy*, vol. 10, pp. 57–63, 2011.

[3] J. A. Cunha, I.-C. Hsu, J. Pouliot, M. Roach III, K. Shinohara, J. Kurhanewicz, G. Reed, and D. Stoianovici, "Toward adaptive stereotactic robotic brachytherapy for prostate cancer: demonstration of an adaptive workflow incorporating inverse planning and an MR stealth robot," *Minimally Invasive Therapy*, vol. 19, pp. 189–202, 2010.

[4] M. Ho, A. B. McMillan, J. M. Simard, R. Gullapalli, and J. P. Desai, "Toward a meso-scale SMA-actuated MRI-compatible neurosurgical robot," *IEEE Trans. Robotics*, vol. 28, no. 1, pp. 213–222, 2012.

[5] G. S. Fischer, A. Krieger, I. Iordachita, C. Csoma, L. L. Whitcomb, and G. Ficthinger, "MRI compatibility of robot actuation techniques - a comparative study," *Int. Conf. Medical Image Computing and Computer Assisted Intervention*, pp. 509–517, 2008.

[6] C. Bergeles, M. P. Kummer, B. E. Kratochvil, C. Framme, and B. J. Nelson, "Steerable intravitreal inserts for drug delivery: *in vitro* and *ex vivo* mobility experiments," *Int. Conf. Medical Image Computing and Computer Assisted Intervention*, pp. 33–40, 2011.

[7] G. Kósa, P. Jakab, G. Székely, and N. Hata, "MRI driven magnetic microswimmers," *J. Biomedical Microdevices*, pp. 1–14, 2011.

[8] A. Chanu, O. Felfoul, G. Beaudoin, and S. Martel, "Adapting the clinical MRI software environment for real-time navigation of an endovascular untethered ferromagnetic bead for future endovascular interventions," *Magnetic Resonance in Medicine*, vol. 59, pp. 1287–1297, 2008.

[9] P. Vartholomeos, L. Qin, and P. E. Dupont, "MRI-powered actuators for robotic interventions," *IEEE/RSJ Int. Conf. Intelligent Robots and Systems*, pp. 4508–4515, 2011.

[10] R. van der Weide, C. J. G. Bakker, and M. A. Viergever, "Localization of intravascular devices with paramagnetic markers in MR images," *IEEE Trans. Biomedical Engineering*, vol. 20, no. 10, pp. 1061–1071, 2001.

[11] H. Busse, R. Trampel, W. Gruünder, M. Moche, and T. Kahn, "Method for automatic localization of MR-visible markers using morphological image processing and conventional pulse sequences: feasibility for image-guided procedures," *J. Magnetic Resonance Imaging*, vol. 28, pp. 1087–1096, 2007.

[12] M. Moche, R. Trampel, T. Kahn, and H. Busse, "Navigation concepts for MR image-guided interventions," *J. Magnetic Resonance Imaging*, vol. 27, pp. 276–291, 2008.

[13] C. L. Dumoulin, S. P. Souza, and R. D. Darrow, "Real-time position monitoring of invasive devices using magnetic resonance," *Magnetic Resonance in Medicine*, vol. 29, pp. 411–415, 1993.

[14] J. M. Santos, G. A. Wright, and J. M. Pauly, "Flexible real-time magnetic resonance imaging framework," *IEEE Int. Conf. Engineering in Medicine and Biology*, pp. 1048–1051, 2004.